

Utilizing Principal Component Analysis on Multispectral Aerial Imagery for Identification of Underlying Structures

Marcos Bosques-Perez, Walter Izquierdo, Harold Martin, Liangdon Deng, Josue Rodriguez, Thony Yan, Mercedes Cabrerizo, Armando Barreto, Naphtali Rische, and Malek Adjouadi

Abstract—Aerial imagery is a powerful tool when it comes to analyzing temporal changes in ecosystems and extracting valuable information from the observed scene. It allows us to identify and assess various elements such as objects, structures, textures, waterways, and shadows. To extract meaningful information, multispectral cameras capture data across different wavelength bands of the electromagnetic spectrum. In this study, the collected multispectral aerial images were subjected to principal component analysis (PCA) to identify independent and uncorrelated components or features that extend beyond the visible spectrum captured in standard RGB images. The results demonstrate that these principal components contain unique characteristics specific to certain wavebands, enabling effective object identification and image segmentation.

Keywords—big data, image processing, multispectral, principal component analysis.

I. INTRODUCTION

THE technological advancements of the past have undeniably improved the overall quality of life in society. However, these advancements have also led to negative impacts on our ecosystem, resulting in serious consequences such as climate change, global warming, rising sea levels, extreme weather events, and air and sea pollution [1].

To assess the effects of these consequences, one effective approach is the use of multispectral aerial imaging, which involves capturing aerial imagery from unmanned aerial vehicles (UAVs) and analyzing temporal changes reflected in different wavelength bands of the electromagnetic spectrum. A significant challenge faced with multispectral images is the presence of clouds or haze caused by pollution. Clouds and gases can obstruct parts of the scene or reduce visibility due to light refraction, altering the way the camera perceives ground colors [2]-[5].

Brauers et al. [6] affirm that multispectral cameras offer superior color fidelity compared to RGB cameras, thanks to their different methods of color acquisition with dedicated filters. But, obtaining these images is difficult in their own right because of the spatial resolution [7], [8]. Given these challenges, there is a need to find new ways to obtain more informative multispectral images that fully utilize the information in their respective wavebands. These multispectral images encompass 8 bands of color information compared to the standard three channels of the RGB model, which opens

possibilities for incorporating both qualitative and quantitative aspects of the analysis [9].

This study proposes using principal component analysis (PCA) to identify all independent and uncorrelated components in multispectral aerial images and understand their potential implications for different elements within the scene. [10]-[12] Once the green areas, trees, waterways, buildings, roadways, roofs, etc., have been extracted, it becomes possible to assess the damage caused by extreme weather events, such as destruction, flooding, and fallen trees, by comparing the scenes before and after the event. Additionally, longitudinal studies of multispectral aerial imagery enable the assessment of the lasting effects of global warming and sea level rise on various areas viewed through multispectral imaging.

By separating multispectral images into their principal components, we can ascertain the contribution of each independent component in extracting or segmenting specific elements of the scene, leading to valuable insights into environmental monitoring and understanding the impact of human activities on our ecosystem.

II. DATA

The dataset utilized for evaluating the proposed approach consisted of multispectral aerial imagery obtained from the WorldView-3 satellite, provided by Geoimage. The specific image used in this study captures the city of Adelaide, South Australia, as shown in Figure 1. Table 1 presents a summary of the bands captured by the satellite sensor, including their respective names, wavelengths, and resolutions, as provided by Geoimage company[13]. The dimensions of the image are 4259x4277x8 pixels, with each pixel containing information up to a 16-bit integer representation.

III. METHODOLOGY

A. Pre-processing

In this study, we utilized the MatLab R2023a platform to transform the aerial image from a three-dimensional matrix ($M \times N \times K$) to a two-dimensional matrix ($MN \times K$). To change the matrix dimension, we employed a column-by-column flattening technique, wherein we traversed the matrix by columns and concatenated the elements into a single-dimensional vector. This process was applied to all 8 bands, resulting in 8 one-dimensional vectors that were subsequently arranged into a two-dimensional matrix. This step was necessary since

TABLE I
WORLDVIEW-3 BANDS

Number	Name	Wavelength (μm)	Resolution (m)
1	Coastal	0.400-0.450	1.24
2	Blue	0.450-0.510	1.24
3	Green	0.510-0.580	1.24
4	Yellow	0.585-0.625	1.24
5	Red	0.630-0.690	1.24
6	Red Edge	0.705-0.745	1.24
7	NIR1	0.770-0.895	1.24
8	NIR2	0.860-1.040	1.24

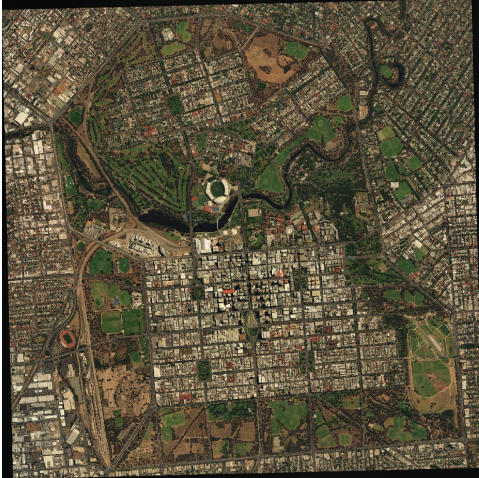


Fig. 1. Original image from WorldView-3 of Adelaide, South Australia in full detail.

MatLab requires a two-dimensional matrix for performing PCA. The resulting matrix size has a total of 18,215,743 pixels for each of the 8 bands.

B. Principal Component Analysis

To initiate the PCA process, the mean vector μ of the columns is computed to center the data. The mean-adjusted matrix is obtained by subtracting this mean vector from the original data. Then, eigenvectors and eigenvalues are computed using the EIG decomposition method. Prior to the decomposition, the covariance matrix of the image needs to be calculated. Equation 1 illustrates the procedure for computing the covariance matrix, where X_0 represents the mean-adjusted matrix.

$$C_{X_0} = X_0 X_0^T \quad (1)$$

With our dataset, the covariance matrix would be 8x8 dimensions. With this covariance, we obtain the eigenvalues which are an 8-element vector, and the eigenvectors which are an 8x8 matrix. After ordering our eigenvectors using the eigenvalues in the descending method, we are able now to perform the transformation into principal components. To do this, we multiply our mean-adjusted matrix (X_0) with the eigenvectors (A) as given in equation 2.

$$Y = X_0 A \quad (2)$$

TABLE II
PCA SUMMARY

Number	Explained (%)	Eigenvalue ($\times 10^5$)
1	74.567	4.037
2	22.341	1.210
3	1.305	0.071
4	0.904	0.049
5	0.464	0.025
6	0.194	0.011
7	0.173	0.009
8	0.053	0.003

To present the image accurately, we need to restore the matrix dimensions to their original size by performing the reverse flattening process as seen above. Each of the 8 bands now corresponds to a principal component.

IV. RESULTS

We analyze our principal components and assess the percentage of information each component contributes to the entire image. Table II provides these percentages, and the eigenvalues for each component arranged in descending order. The first two principal components already capture more than 95% of the information contained in the image. However, we note that the components containing the remaining 5% should not be underestimated, as they could still contain relevant characteristics or features in the analysis of the viewed scene.

In addition to analyzing the principal components through a table, we also generate visual representations of each principal component as images. Figure 2 depicts each principal component individually. By visually examining principal components 1 and 2, we can validate the findings presented in Table II. On the other hand, the remaining principal components appear to contain minimal to no information, as evident from the lack of discernible details.

However, upon closer examination by zooming in on these images, intriguing features or patterns that were initially unnoticed can be revealed. This phenomenon is particularly evident when analyzing principal component 2. Figure 3 provides a comparison between principal component 2 and the original image, focusing on the same area. Initially, in the original image, the region surrounding the orange square appears to be a typical grassy area. However, a closer inspection of principal component 2 indicates that it does not possess the same color as other grassy areas, as evidenced by the regions within the red square. Instead, upon observing the areas within the blue square, we can observe that it shares the same color as the river. In other words, the green circular area in the original image, which was presumed to be grass, is in fact water. Upon verifying through Google Maps, it was confirmed that this is a pond named Model Boat Pond.

This is not the only principal component that demonstrates such behavior. By examining principal component 4, we also discover some fascinating insights. Figure 4 illustrates how this component emphasizes objects with significant reflection. In this specific instance, two buildings reflect the rays of the sun,

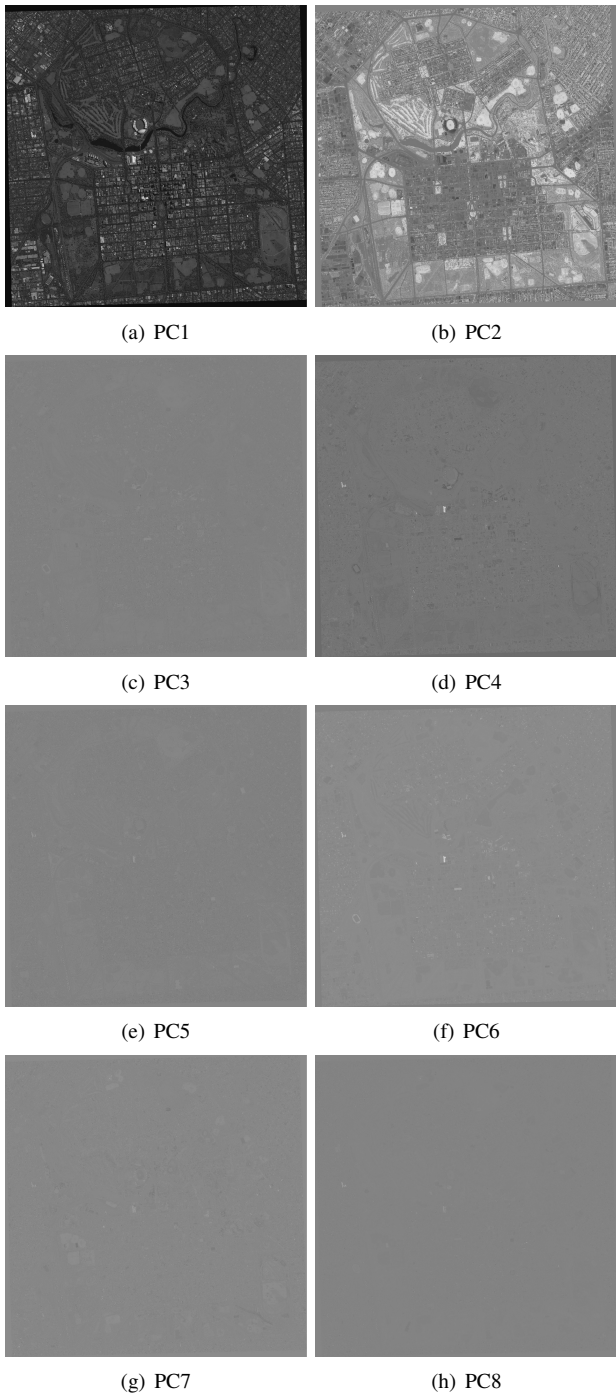


Fig. 2. Representation of all 8 principal components of the original image

and these reflections are prominently visible in the principal component.

As indicated in Table II, principal component 3 contributes slightly over 1% of the overall image information. However, what makes this small portion of information intriguing is its content. Upon zooming in on the roads within the image, one can observe the presence of small rectangles that consistently follow a specific pattern - a combination of white or gray with a black dot at one end. Upon comparing these rectangles with the original image, it becomes evident that they represent vehicles on the road. Figure 5 visually presents the comparison

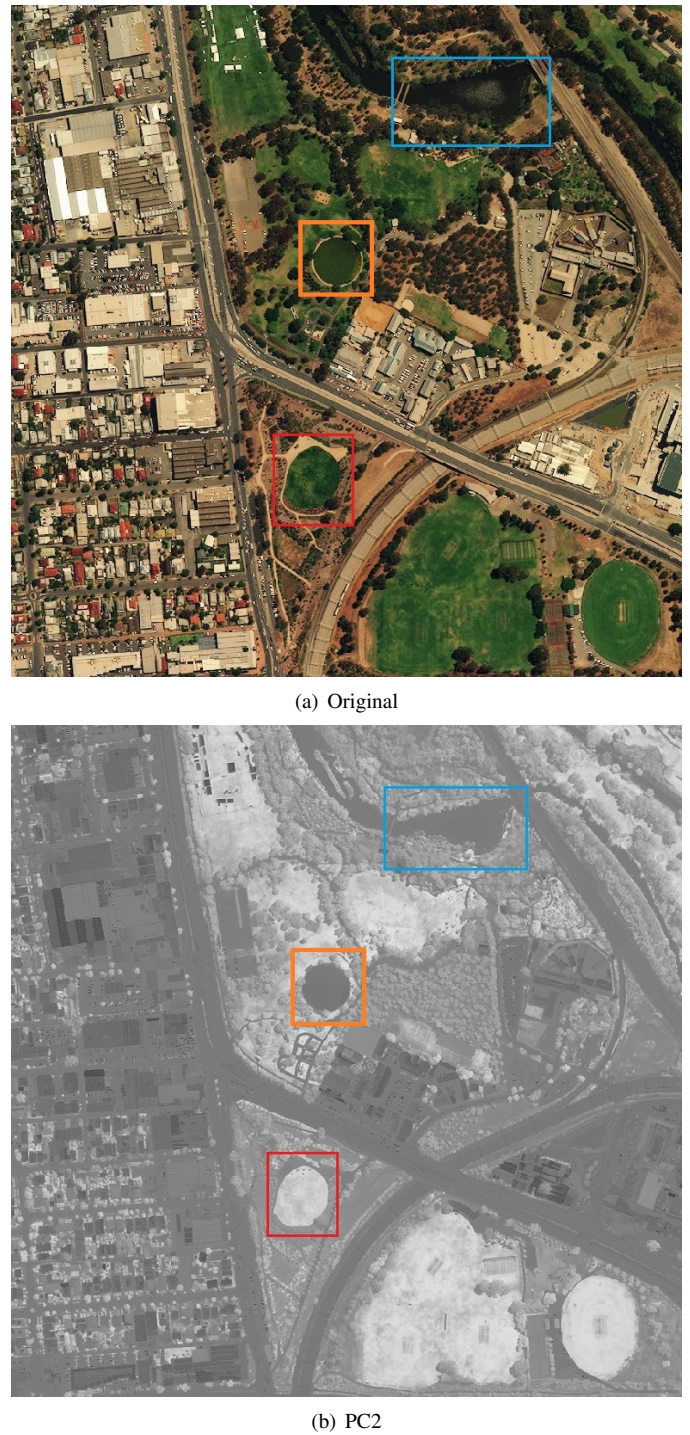
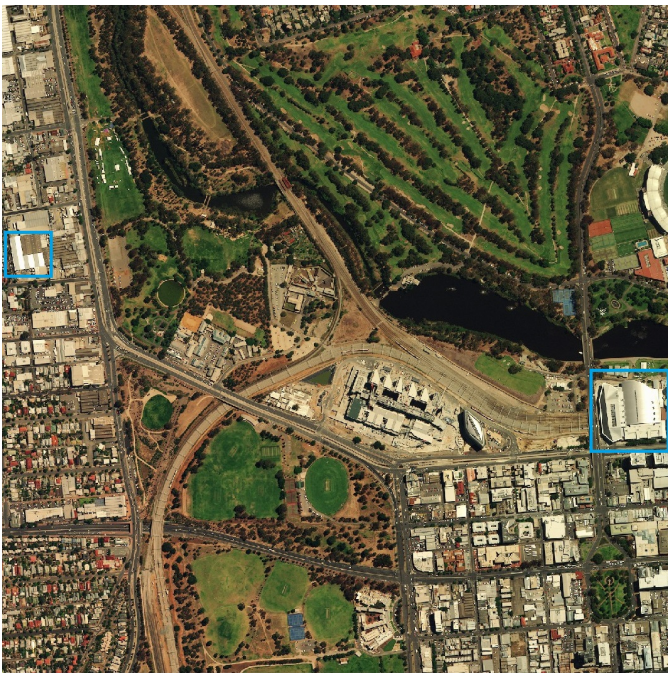


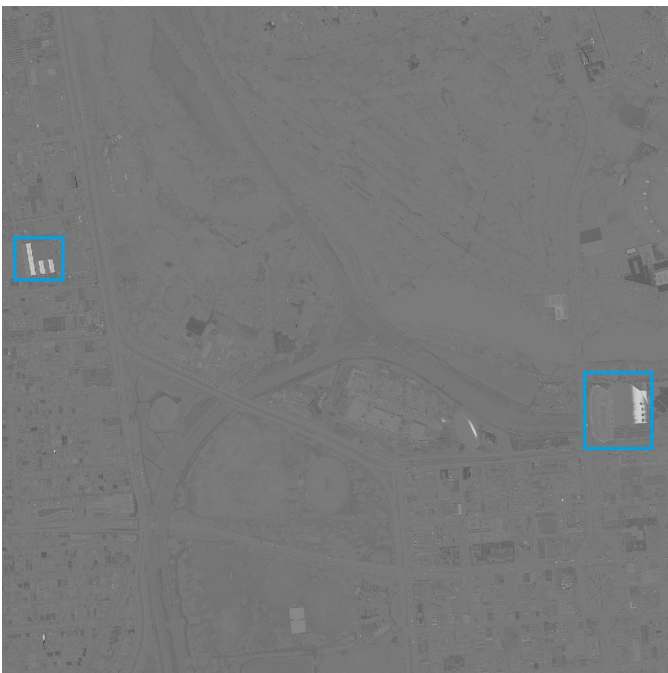
Fig. 3. Comparison between the original image and principal component 2

and representation of these vehicle rectangles.

Lastly, a single principal component can assist in identifying multiple objects or structures within an image. This is exemplified by principal component 2, which not only aids in identifying water bodies but also helps to identify trees. Remarkably, these trees can be observed even in proximity to buildings or within the shadows of other structures. Figure 6 highlights areas within red squares where trees, which were inconspicuous in the original image, become apparent with the assistance of principal component 2.



(a) Original



(b) PC4

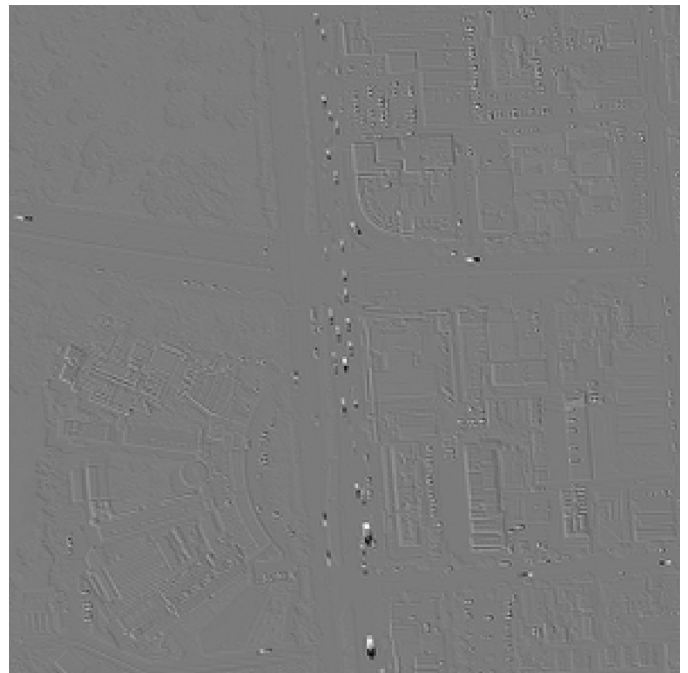
Fig. 4. Comparison between the original image and principal component 4

V. CONCLUSION

The results obtained with the proposed PCA-based approach demonstrate that each principal component contains relevant information for identifying specific structures in the multispectral images, such as water bodies, trees, green areas, and the different urban structures. The merits of this research extend to resolving ambiguous situations, such as green pond water vs. green areas, and for extracting objects in shaded areas, that standard image segmentation techniques would fail to resolve. Our research group is working to expand and augment the



(a) Original



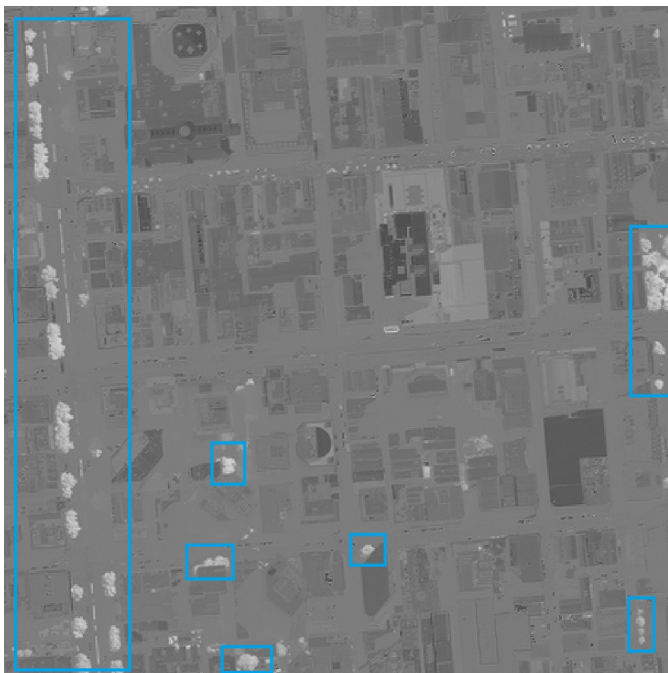
(b) PC3

Fig. 5. Comparison between the original image and principal component 3

present method by incorporating the independent component analysis (ICA) to address added variability in the images and the challenging issues of the multispectral nature of fog and clouds. The first finding, in terms of fog and clouds, is that they contribute to more than a single PCA component, and a future research endeavor is to determine the extent and weight of their contributions to the different PCA components before their successful removal to reveal the hidden scenery and structures.



(a) Original



(b) PC2

Fig. 6. Comparison between the original image and principal component 2

ACKNOWLEDGMENT

This research is supported by the National Science Foundation under grants: CNS-2018611, CNS-1920182, and CNS-1551221. We also acknowledge the support of the Ware Foundation.

REFERENCES

[1] S. Kovbasiuk, L. Kanevskyy and M. Romanchuk, "Object Detection Method Based on Aerial Image Instance Segmentation by Unmanned Aerial System in the Framework of Decision Making System," 2019

3rd International Conference on Advanced Information and Communications Technologies (AICT), Lviv, Ukraine, 2019, pp. 332-335, doi: 10.1109/AIACT.2019.8847875.

[2] Z. Song, H. Zhang, F. Liu, S. Chen and F. Zhang, "Unmanned Aerial Vehicle Coverage Path Planning Algorithm Based on Cellular Automata," 2018 International Conference on Information Systems and Computer Aided Education (ICISCAE), Changchun, China, 2018, pp. 371-374, doi: 10.1109/ICISCAE.2018.8666895.

[3] I. Yoon, M. H. Hayes and J. Paik, "Wavelength-adaptive image formation model and geometric classification for defogging unmanned aerial vehicle images," 2013 IEEE International Conference on Acoustics, Speech and Signal Processing, Vancouver, BC, Canada, 2013, pp. 2454-2458, doi: 10.1109/ICASSP.2013.6638096.

[4] P. Duan, S. Hu, X. Kang and S. Li, "Shadow Removal of Hyperspectral Remote Sensing Images With Multiexposure Fusion," in IEEE Transactions on Geoscience and Remote Sensing, vol. 60, pp. 1-11, 2022, Art no. 5537211, doi: 10.1109/TGRS.2022.3203808.

[5] Y. Chen, Q. Weng, L. Tang, X. Zhang, M. Bilal and Q. Li, "Thick Clouds Removing From Multitemporal Landsat Images Using Spatiotemporal Neural Networks," in IEEE Transactions on Geoscience and Remote Sensing, vol. 60, pp. 1-14, 2022, Art no. 4400214, doi: 10.1109/TGRS.2020.3043980.

[6] J. Brauers and T. Aach, "Longitudinal aberrations caused by optical filters and their compensation in multispectral imaging," 2008 15th IEEE International Conference on Image Processing, San Diego, CA, USA, 2008, pp. 525-528, doi: 10.1109/ICIP.2008.4711807.

[7] C. Iturrino, F. X. Arias, H. Sierra and E. Arzuaga, "Single-Shot Multispectral Image Acquisition for Low-Altitude Remote Sensing using Light Diffraction Techniques," 2019 10th Workshop on Hyperspectral Imaging and Signal Processing: Evolution in Remote Sensing (WHISPERS), Amsterdam, Netherlands, 2019, pp. 1-5, doi: 10.1109/WHISPERS.2019.8920879.

[8] Z. -W. Pan and H. -L. Shen, "Multispectral Image Super-Resolution via RGB Image Fusion and Radiometric Calibration," in IEEE Transactions on Image Processing, vol. 28, no. 4, pp. 1783-1797, April 2019, doi: 10.1109/TIP.2018.2881911.

[9] W. J. Cukierski, Xin Qi and D. J. Foran, "Moving beyond color: The case for multispectral imaging in brightfield pathology," 2009 IEEE International Symposium on Biomedical Imaging: From Nano to Macro, Boston, MA, USA, 2009, pp. 1111-1114, doi: 10.1109/ISBI.2009.5193251.

[10] S. Xiaorui and W. Lingda, "Denoising of Hyperspectral Images Based on Principal Component Analysis and Adaptive Sparse Coding," 2018 10th IAPR Workshop on Pattern Recognition in Remote Sensing (PRRS), Beijing, China, 2018, pp. 1-6, doi: 10.1109/PRRS.2018.8486272.

[11] M. Kusban, A. Susanto and O. Wahyunggoro, "Feature extraction for palmprint recognition using kernel-PCA with modification in Gabor parameters," 2016 1st International Conference on Biomedical Engineering (IBIOMED), Yogyakarta, Indonesia, 2016, pp. 1-6, doi: 10.1109/IBIOMED.2016.7869820.

[12] G. Zhou, W. Chen, J. A. Kelmelis and D. Zhang, "A comprehensive study on urban true orthorectification," in IEEE Transactions on Geoscience and Remote Sensing, vol. 43, no. 9, pp. 2138-2147, Sept. 2005, doi: 10.1109/TGRS.2005.848417.

[13] "About worldview-3 I A satellite with unsurpassed accuracy & agility," Geoimage, <https://www.geoimage.com.au/satellites-sensors/worldview-3/> (accessed May 22, 2023).